International Journal of Mechanical Sciences 210 (2021) 106743

Contents lists available at ScienceDirect

International Journal of Mechanical Sciences

journal homepage: www.elsevier.com/locate/ijmecsci

Constitutive modeling and numerical simulations for dynamic strain aging in MMFX steel at elevated temperatures

Yooseob Song [a], Jaeheum Yeon [b], George Z. Voyiadjis [c,*]

[a] Department of Civil Engineering, The University of Texas Rio Grande Valley, Edinburg, TX 78539, USA
[b] Department of Regional Infrastructure Engineering, Kangwon National University, Chuncheon, Gangwon-do, 24341, South Korea
[c] Department of Civil and Environmental Engineering, Computational Solid Mechanics Laboratory, Louisiana State University, Baton Rouge, LA 70803, USA

ARTICLE INFO

Keywords:
Dynamic strain aging
MMFX steel
Constitutive modeling
FEM
Model validation

ABSTRACT

The mechanical behavior of Martensitic Microcomposite Formable Steel alloy for a wide range of temperatures from room temperature to 923K and strain rates from 0.0015s^{-1} to 500s^{-1} is investigated focusing on the effect of dynamic strain aging. A new constitutive model including an additional flow stress component due to the dynamic strain aging induced hardening is proposed for Martensitic Microcomposite Formable Steel alloy, which has not been nonexistent so far. A Weibull distribution probability density type function is introduced to describe this hardening. The dynamic strain aging stress element is defined as a function of temperature, equivalent plastic strain, and its rate since its occurrence and characteristics depend on those factors. To check the validity of the proposed model, experimental data from quasi-static and dynamic loading tests in the literature are utilized. The new finite element code corresponding to the proposed model is also developed and validated using experimental data. Lastly, strain rate sensitivity is discussed to investigate the effect of dynamic strain aging.

1. Introduction

Martensitic Microcomposite Formable Steel (MMFX) alloy is an innovative material widely used in structural applications due to its outstanding corrosion resistance, low maintenance cost, and high yield strength [15, 52, 65]. In addition, MMFX has a high ductility, and structures made of this material have a long service life of more than a hundred years [40]. Despite its fast-growing demand for real-world applications, most of the research regarding this material has been focused on its corrosion resistance [12, 19, 40, 41]. In addition, although diverse types of constitutive models have been proposed to investigate the mechanical behaviors of diverse materials such as metals and alloys [29, 44, 61], nanopaper [38], polyampholyte gel [54], shape-memory alloys [13, 18, 60], high-entropy alloys [6, 9, 27, 62], elastomers [30, 33, 64], and neo-Hookean material [10, 22, 23], very limited studies have been performed to investigate the mechanical behavior of MMFX, in particular, under extreme loading conditions [1, 14]. Thus, this work explores how MMFX behaves at a wide range of strain rates and temperatures, especially focusing on a specific phenomenon, termed dynamic strain aging (DSA).

DSA typically occurs in metallic materials at combinations of temperatures and strain rates in their specific ranges [4, 8, 24–26, 31, 32, 47, 63]. It is well known that DSA is caused by the interaction of diffusing solute atoms with mobile dislocations and it induces hardening. Flow stress has a tendency to decrease with temperature rise, however, this additional hardening due to DSA forms a bell-shaped (concave downward) curve in flow stress versus temperature graph. The magnitude of the DSA-induced hardening depends on temperature range, applied strain rate, and strain level. One manifestation of the DSA phenomenon is the serrated stress flow [related to the Portevin-Le Chatelier (PLC) effect] during mechanical testing. Another manifestation is the bell-shaped peak in the flow stress versus temperature curves (the third-type strain aging effect) [46, 58].

There are several undesirable material characteristics associated with DSA such as reduction in fracture resistance and loss of ductility [4, 7]. More details about the physics and characteristics of DSA can be found in the literature [3, 4, 17, 20, 21, 28, 35, 37, 58]. Therefore, it is scientifically and technologically important to understand DSA and its mechanism for a better quality of materials [42, 45]. However, the fundamental mechanics of DSA is still unclear despite extensive research on DSA for the last decades, and more study is required focusing on theoretical and numerical approaches.

In the third author's recent work [1], quasi-static and dynamic tests

* Corresponding author.
E-mail address: voyiadjis@eng.lsu.edu (G.Z. Voyiadjis).

https://doi.org/10.1016/j.ijmecsci.2021.106743
Received 7 June 2021; Received in revised form 1 August 2021; Accepted 13 August 2021
Available online 15 August 2021

at a broad range of strain rates ($\dot{\varepsilon} = 0.0015 - 500\ s^{-1}$) were performed with MMFX cylindrical samples at four temperatures ($T = 298, 523, 723, 923K$). Average chemical composition of MMFX was revealed as follows through wet chemical analysis: Fe (balance), Cr (9.6 %), Mn (1.1 %), Si (0.5 %), C (0.15 %) [1]. It was shown that DSA becomes active at $500\ K \lesssim T \lesssim 900\ K$ under $\dot{\varepsilon} = 0.0015$ and $\dot{\varepsilon} = 0.15\ s^{-1}$ and at all strain levels from yield strain to $\varepsilon = 0.05$. The physically based Voyiadjis-Abed constitutive model (VA model) was employed in their work to investigate the plastic flow of MMFX alloys, however, it did not address the DSA-induced hardening.

In the current work, a new temperature- and rate-dependent constitutive model is proposed to investigate mechanics of MMFX under extreme environments focusing on the third-type strain aging effect by combining an additional component describing the DSA-induced hardening with the existing VA model. The proposed model is then validated using the experiments, which were performed by Abed et al. [1]. The VA model consists of athermal (σ_a) and thermal (σ_{th}) flow stress components, and the additional component for DSA (σ_d) is expressed by a function of temperature, equivalent plastic strain (ε_p), and equivalent plastic strain rate ($\dot{\varepsilon}_p$) through a probability density type function. A negligibly small elastic deformation is assumed, therefore the following assumption is made in this work: $\varepsilon = \varepsilon_p$ and $\dot{\varepsilon} = \dot{\varepsilon}_p$. This concept has been utilized over the recent years in the authors' works to study the effect of DSA for the following materials: titanium [51], Inconel 718 alloy [56], C45 steel [57], niobium [50], and Q235B steel [49]. Finite element (FE) code corresponding to the proposed model is also developed in this work. To define an isotropic yield behavior of MMFX, a user-defined subroutine is written and called at all material calculation element points. The developed FE code is then validated using the experimental measurements by Abed et al. [1].

The outline of this work is as follows. In Section 2, a new type of constitutive model is proposed by incorporating the effect of DSA hardening. In Section 3, material parameters for the proposed model are calibrated using experimental data. In Section 4, the FE code for the proposed model is introduced. In Section 5, the proposed model and its FE code are validated by comparing them to experimental stress-strain responses. In Section 6, strain rate sensitivity, one of the important issues caused by DSA, is discussed. The findings of this work are summarized in Section 7. Note that the terms "stress" and "strain" stand for "true stress" and "true strain" in this work unless stated otherwise.

2. Constitutive model

As introduced in the previous section, the total flow stress (σ) in the proposed model is composed of the three elements, i.e.

$$\sigma = \sigma_a + \sigma_{th} + \sigma_d \tag{1}$$

where the first, second, and third terms denote the athermal, thermal, and DSA stresses, respectively. The VA model consists of the first two components in Eq. (1), i.e. $\sigma = \sigma_a + \sigma_{th}$, without the DSA hardening. It has been shown in many literatures that constitutive models without considering the effect of DSA (including the VA model) are not able to provide a good quality of predictions [9, 43, 49, 57]. Note that grain boundary strengthening is not considered in this work.

Generally, short-range barrier and long-range barrier are two kinds of barriers to obstruct the movement of dislocations in crystal lattices. The former is overcome by thermal activation energy whereas the latter is not. An additive decomposition of the athermal and thermal elements is established based on this, and its validity was demonstrated in several works [49–51, 55–57].

For MMFX steel in the current model, σ_a is defined as a function of ε_p, and σ_{th} is defined as a function of ε_p, $\dot{\varepsilon}_p$ and T as follows:

$$\sigma_a\left(\varepsilon_p\right) = \overline{\sigma}_a + B\varepsilon_p^{n_1} \tag{2}$$

$$\sigma_{th}\left(\varepsilon_p,\ \dot{\varepsilon}_p,\ T\right) = \overline{\sigma}_{th}\varepsilon_p^{n_2}\left(1 - \left(\beta_1 T - \beta_2 T\frac{\dot{\varepsilon}_p}{\dot{\varepsilon}_p^0}\right)^{\frac{1}{q}}\right)^{\frac{1}{p}} \tag{3}$$

where $\overline{\sigma}_a$ denotes the athermal yield stress, and B and n_1 define the athermal hardening. The thermal yield stress is defined by $\overline{\sigma}_{th}$ and n_2. $\dot{\varepsilon}_p^0$ is the referential equivalent plastic strain rate, and it is set as 1.0 in this work. The constants β_1, β_2, p, and q need to be determined by curve fitting using experimental measurements. Typically, $p \in [0: 1]$ and $q \in [1: 2]$. In the current work, it is assumed $p = 0.5$ and $q = 1.5$.

DSA may cause instabilities including temporal and spatial instabilities (loss of homogeneity of strain) during plastic deformation mostly in metallic materials [26, 39, 51, 56]. The dislocations motion in materials is not a continuous procedure. In plastic flow, dislocations run into obstacles, and their movements are stopped temporally. The diffusion of solutes occurs around the trapped dislocations, and additional sufficient stress is required to move to another adjacent dislocation. This process is repeated during plastic deformation. The occurrence of DSA is thus attributed to the interaction between diffusing solute elements and mobile dislocations [11]. Fig. 1 shows this process schematically. During deformation, solute atoms are forced through lattice structures. It creates mobile dislocations remaining pinned at other dislocations until they are dislodged by an adequate level of stress. The waiting time (t_w) represents the amount of time that dislocations remain pinned. When t_w gets close to the aging time, DSA becomes activated [36].

Meanwhile, the following equation is utilized in this work to connect the dislocation density with the equivalent plastic strain [5]:

$$\frac{d\rho}{d\varepsilon_p} = U - A - \Omega\rho \tag{4}$$

where U is the rate of dislocations annihilation, A is the rate of mobile dislocations annihilation and Ω is related to the probability of immobile dislocations annihilation.

The dislocation density, ρ, is then obtained by

$$\rho = \frac{U - A}{\Omega}\left[1 - \exp\left(-\Omega\varepsilon_p\right)\right] + \rho_0\exp\left(-\Omega\varepsilon_p\right) \tag{5}$$

where ρ_0 is the initial dislocation density.

The effect of DSA on flow stresses was investigated in Bergstrom and Roberts [5] by comparing model predictions with experiments as shown

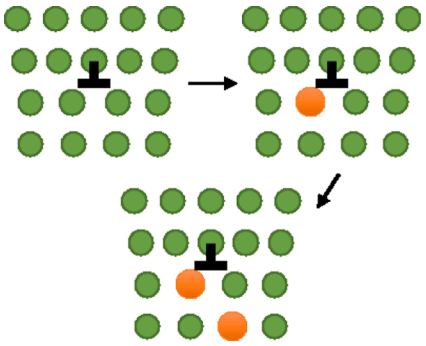

Fig. 1. Schematic illustration for the DSA process. During DSA, substitutional impurities (indicated by orange circles) are driven across the slip plane. The interaction between solute atoms and lattice dislocations occurs when the former enters crystalline solids, and it may change the material behavior. Solute atoms cluster below the dislocations and form Cottrell atmospheres, which restrict the motion of dislocations and hold them in place [11]. The additional stress is required to move the dislocations caught by the atmospheres, and this causes an increase in strength. The term "aging" refers to the process of solutes diffusing towards dislocations over time [16].

in Fig. 2. In Fig. 2(a), an increase in yield stress is observed at a certain range of temperatures. Correspondingly, at the same temperature range, relatively large values of $U - A$ (Fig. 2(b)) and low values of Ω (Fig. 2(c)) were observed as well. Based on this finding, an increase in flow stress can be obtained by the substitution of Eq. (5) into Taylor's dislocation model ($\sigma = \alpha\mu b\sqrt{\rho}$) [53].

$$\sigma = \sigma_0 + \alpha\mu b\left\{\frac{U-A}{\Omega}\left[1-\exp\left(-\Omega\varepsilon_p\right)\right] + \rho_0\exp\left(-\Omega\varepsilon_p\right)\right\}^{1/2} \tag{6}$$

where σ_0 is the friction stress and μ is the shear modulus. It can be concluded that DSA could be modeled through a form of probability function because it has a probabilistic nature.

Based on the aforementioned concept, the following functional form of a Weibull distribution probability density function is employed in this work as a function of equivalent plastic strain and temperature to characterize σ_d:

$$\sigma_d = a_d exp\left[-\frac{\{T - \mathscr{W}\}^2}{b_d}\right] \tag{7}$$

where the terms $a_d > 0$ and $b_d > 0$ determine the scale and shape of σ_d. The former defines the magnitude of DSA-induced hardening, whereas the latter defines a range of temperatures where the DSA hardening is present. The term $\mathscr{W}$ is associated with the temperature at which the relationship between mobile dislocations and solute atoms becomes most concentrated.

The terms a_d and b_d are defined as a function of ε_p, respectively. Since there are three available data sets with different levels of ε_p [1], a unique expression can be defined for a_d and b_d if a power-law form is employed. Thus, the terms a_d and b_d are defined in the following forms:

$$a_d\left(\varepsilon_p\right) = \overline{a}\varepsilon_p^{n_a} \tag{8}$$

$$b_d\left(\varepsilon_p\right) = \overline{b}\varepsilon_p^{n_b} \tag{9}$$

where the material constants (k_a and k_b) and the law's exponents (n_a and n_b) need to be calibrated. Note that other functional forms may be used for a_d and b_d [56, 57].

The function $\mathscr{W}$, on the other hand, is given as a function of $\dot{\varepsilon}_p$. Only two data sets are available for defining this function, as a result, it cannot be defined uniquely [1]. Some feasible forms are power-law, linear, and logarithmic such as

$$\begin{aligned}
&(\text{power}-\text{law})\ \ \mathscr{W}\left(\dot{\varepsilon}_p\right) = \overline{\mathscr{W}}\dot{\varepsilon}_p^{n_{\mathscr{W}}}\\
&(\text{linear})\ \ \mathscr{W}\left(\dot{\varepsilon}_p\right) = \overline{\mathscr{W}}\dot{\varepsilon}_p + \overline{\overline{\mathscr{W}}}\\
&(\text{logarithmic})\ \ \mathscr{W}\left(\dot{\varepsilon}_p\right) = \overline{\mathscr{W}}\ln\dot{\varepsilon}_p + \overline{\overline{\mathscr{W}}}
\end{aligned} \tag{10}$$

where $\overline{\mathscr{W}}$, $\overline{\overline{\mathscr{W}}}$, and $n_{\mathscr{W}}$ are the material constants that need to be calibrated.

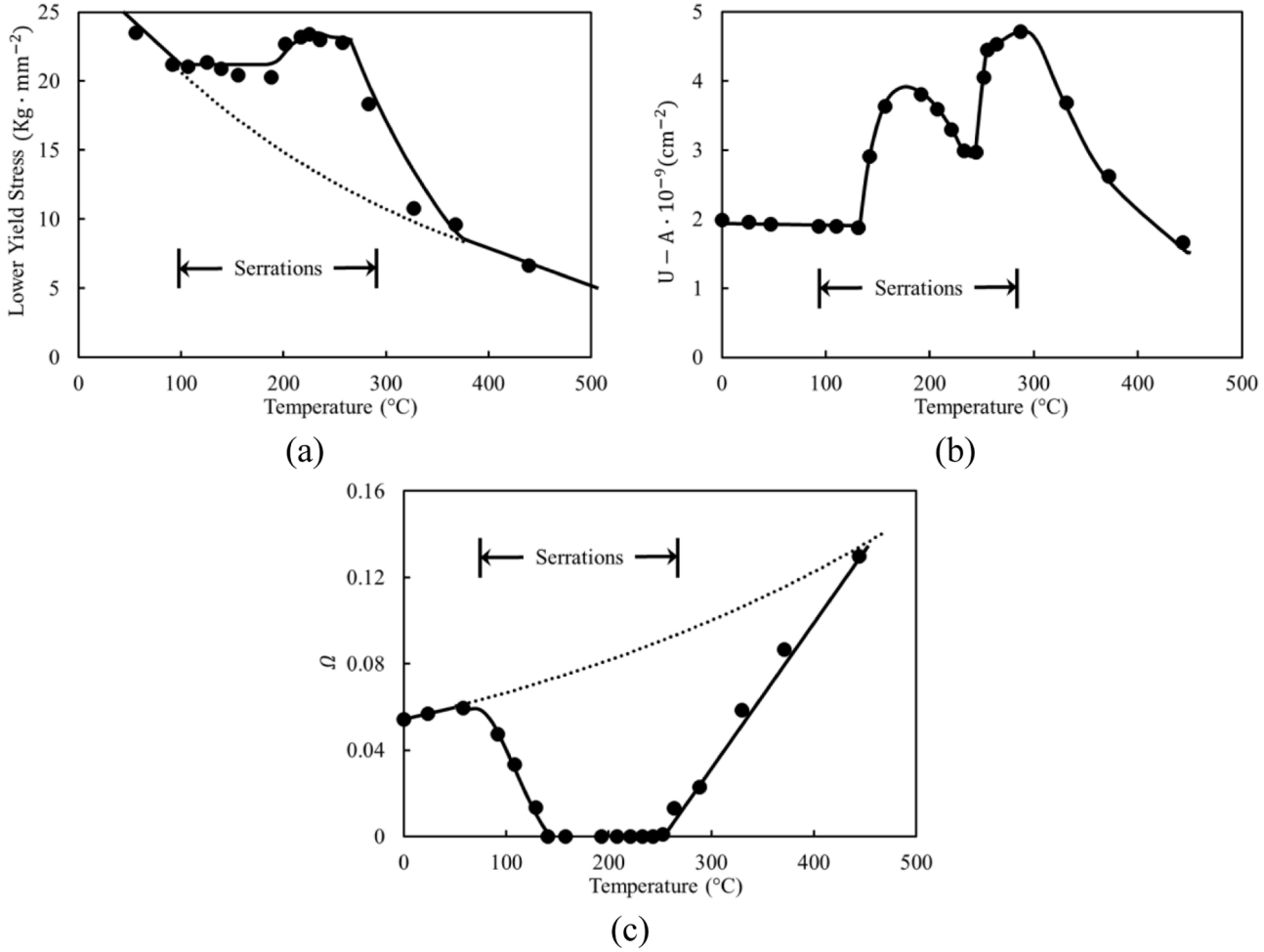

Fig. 2. Graphs of (a) lower yield stress (units: $kg \bullet mm^{-2}$), (b) $U - A$ (units: $10^{-9} \bullet cm^{-2}$) and (c) Ω as a function of temperature. Solid lines and dots represent model predictions and experimental data, respectively [5]. The dashed lines indicate the expected results without the effect of DSA.

3. Calibration for the model parameters

The parameters for the proposed model are calibrated using the experimental measurements on stress-temperature responses at several levels of equivalent plastic strain and equivalent plastic strain rate. For this purpose, in Abed et al. [1], a universal testing machine (UTM) and dynamic drop mass bench were used to perform quasi-static uniaxial tensile tests ($\dot{\varepsilon} = 0.0015$, 0.015, and $0.15s^{-1}$) and drop hammer dynamic tests ($\dot{\varepsilon} =$ 300, 400, and $500s^{-1}$). Zwick/Roell 3-zone high-temperature furnace was also used along with a UTM to test the materials at elevated temperatures ($T = 523, 723, 923K$). See Abed et al. [1] for more information about the experimental setup.

Flow stress tends to decline with temperature rise up to a certain temperature (called a critical temperature) and remains unchanged beyond the critical temperature. This level of constant flow stress indicates the athermal flow stress. In this work, the highest temperature employed in this work, $923K$, is assumed as the critical temperature because the experiments were performed up to that temperature and there is no available data. The three athermal stress parameters ($\overline{\sigma}_a$, B, and n_1) in Eq. (2) are determined first by using stress-strain data at the critical temperature. The parameter $\overline{\sigma}_a$ represents the athermal stress at $\varepsilon_p = 0$.

Next, the material parameters defining thermal stress need to be determined. It can be done by using the relationship, $\sigma_{th} = \sigma - \sigma_a - \sigma_d$. Flow stress versus temperature graphs at different strains are utilized for this step. The two exponent parameters, p and q, are associated with the thermal degradation mechanism. In most of the literature including the authors' previous work [51, 56, 57], $p = 0.5$ and $q = 1.5$ were taken as suitable values because they provide the most accurate results. To obtain $\overline{\sigma}_{th}$ and n_2, $(\sigma - \overline{\sigma}_a - B\varepsilon_p^{n_1} - \sigma_d)^p$ versus $T^{\frac{1}{q}}$ responses at different plastic strain levels with designated strain rates can be utilized. Similarly, $(1 - ((\sigma - \overline{\sigma}_a - B\varepsilon_p^{n_1} - \sigma_d)/\overline{\sigma}_{th}\varepsilon_p^{n_2})^p)^q$versus $\dot{\varepsilon}_p$ graphs at different levels of temperature and plastic strain are employed to determine β_1 and β_2. The determined material parameters of the VA model for MMFX are summarized in Table 1.

The functions in Eq. (7), a_d, b_d, and $\mathscr{W}$, must be defined properly to well capture the DSA hardening. In the experiments [1], bell-shaped (concave downward) curves in stress versus temperature graphs were clearly observed at all levels of strain (yield strain, $\varepsilon_p = 0.02$, and $\varepsilon_p = 0.05$) under quasi-static loadings ($\dot{\varepsilon} = 0.0015$ and $0.15s^{-1}$). The main source of this additional hardening is DSA, and this must be considered when building a constitutive model. Flow stress versus temperature responses can be used to define the expressions for a_d, b_d, and $\mathscr{W}$ for this purpose.

Based on the expressions given in Eqs. (8) and (9) along with the three available experimental data sets at yield strain, $\varepsilon_p = 0.02$ and $\varepsilon_p = 0.05$, the functions a_d and b_d can be accurately defined by comparing the magnitude and width of bell-shaped DSA predicted by the proposed model to the experimentally observed shape and scale of DSA hardening. This is shown in Fig. 3(a). The coefficient of determination, $R^2 = 0.9999$, is obtained for both functions. These functions for MMFX are defined as follows:

$$a_d(\varepsilon_p) = 743\varepsilon_p^{0.0344}\ (MPa) \tag{11}$$

$$b_d(\varepsilon_p) = 61612\varepsilon_p^{0.0695}\ (K^2) \tag{12}$$

Table 1
VA Model parameters for MMFX.

(MPa)	$B(MPa)$	$n_1(-)$	$\overline{\sigma}_{th}\ (MPa)$	$n_2(-)$
100	1000	0.6	3000	0.06
$\beta_1\ (1/K)$	$\beta_2\ (1/K)$	$p(-)$	$q(-)$	$\dot{\varepsilon}_p^0\ (s^{-1})$
7.8×10^{-4}	5.0×10^{-7}	0.5	1.5	1.0

Meanwhile, only two experimental data sets from [1] are available to define $\mathscr{W}$ at $\dot{\varepsilon} = 0.0015\ s^{-1}$ and $0.15s^{-1}$. Various forms including power-law, linear and logarithmic are tested to figure out which one provides the most accurate results (Fig. 3(b)). In terms of accuracy, it is shown that gap is little from each other. Therefore, a power-law form is selected since not only it was used for a_d and b_d, but also it is composed of only one term. $\mathscr{W}$ is defined as follows:

$$\mathscr{W}\left(\dot{\varepsilon}_p\right) = 656\dot{\varepsilon}_p^{-0.009}\ (K) \tag{13}$$

By substituting Eqs. (11), (12), and (13) into Eq. (7), the DSA stress component for MMFX is given as

$$\sigma_d\left(\varepsilon_p,\ \dot{\varepsilon}_p,\ T\right) = 743\varepsilon_p^{0.0344}\exp\left[-\frac{\left\{T - 656\dot{\varepsilon}_p^{-0.009}\right\}^2}{61612\varepsilon_p^{0.0695}}\right] \tag{14}$$

With the calibrated material parameters for the VA model and the defined functions for the DSA hardening, total flow stress is plotted with respect to temperature at yield strain, $\varepsilon_p = 0.02$, and $\varepsilon_p = 0.05$ as shown in Fig. 4. The concave downward bell-shaped hardening is described properly by the proposed model, whereas the VA model without DSA cannot capture it. At $\varepsilon_p = 0.05$ under both strain rates, the proposed model tends to overestimate the flow stresses when compared to the experimental data, especially at elevated temperatures. The reason is that MMFX undergoes a relatively short hardening period, followed by a long softening as temperature increases. This effect is not included in the proposed model.

4. Finite element implementation

The finite element method (FEM) for the proposed model is implemented to demonstrate its numerical validation. Implementing a UHARD subroutine can be the most efficient method to define the hardening parameters for isotropic plasticity and yield surface size. Therefore, the proposed model is implemented via the commercial solver ABAQUS by writing this subroutine. In the subroutine, it is required to define the derivatives of flow stress with respect to equivalent plastic strain, equivalent plastic strain rate, and temperature.

The flow stress in the current model is given as a function of ε_p, $\dot{\varepsilon}_p$ and T. These variables are indicated by `EQPLAS` (ε_p), `EQPLASRT` ($\dot{\varepsilon}_p$) and `TEMP` (T). The flow stress is defined in the subroutine as `SYIELD`. Variables that need to be defined in the subroutine are `HARD(1)` $= \partial\sigma/\partial\varepsilon_p$, `HARD(2)` $= \partial\sigma/\partial\dot{\varepsilon}_p$ and `HARD(3)` $= \partial\sigma/\partial T$. Note that these variables are automatically computed by ABAQUS for each integration point according to the element order and type selected.

The total flow stress is defined as the contribution of four components as follows:

$$\sigma\left(\varepsilon_p,\ \dot{\varepsilon}_p,\ T\right) = \sigma_a(\varepsilon_p) + \sigma_{th}\left(\varepsilon_p,\ \dot{\varepsilon}_p,\ T\right) + \sigma_d\left(\varepsilon_p,\ \dot{\varepsilon}_p,\ T\right) \tag{15}$$

Each term is respectively given by

$$\sigma_a(\varepsilon_p) = \overline{\sigma}_a + B\varepsilon_p^{n_1} \tag{16}$$

$$\sigma_{th}\left(\varepsilon_p,\ \dot{\varepsilon}_p,\ T\right) = \overline{\sigma}_{th}\varepsilon_p^{n_2}\left(1 - \left(\beta_1 T - \beta_2 T\frac{\dot{\varepsilon}_p}{\dot{\varepsilon}_p^0}\right)^{\frac{1}{q}}\right)^{\frac{1}{p}} \tag{17}$$

$$\sigma_d\left(\varepsilon_p,\ \dot{\varepsilon}_p,\ T\right) = a_d(\varepsilon_p)exp\left[-\frac{\left\{T - \mathscr{W}\left(\dot{\varepsilon}_p\right)\right\}^2}{b_d(\varepsilon_p)}\right] \tag{18}$$

The definition of `HARD(1)` can be addressed by decomposing it into:

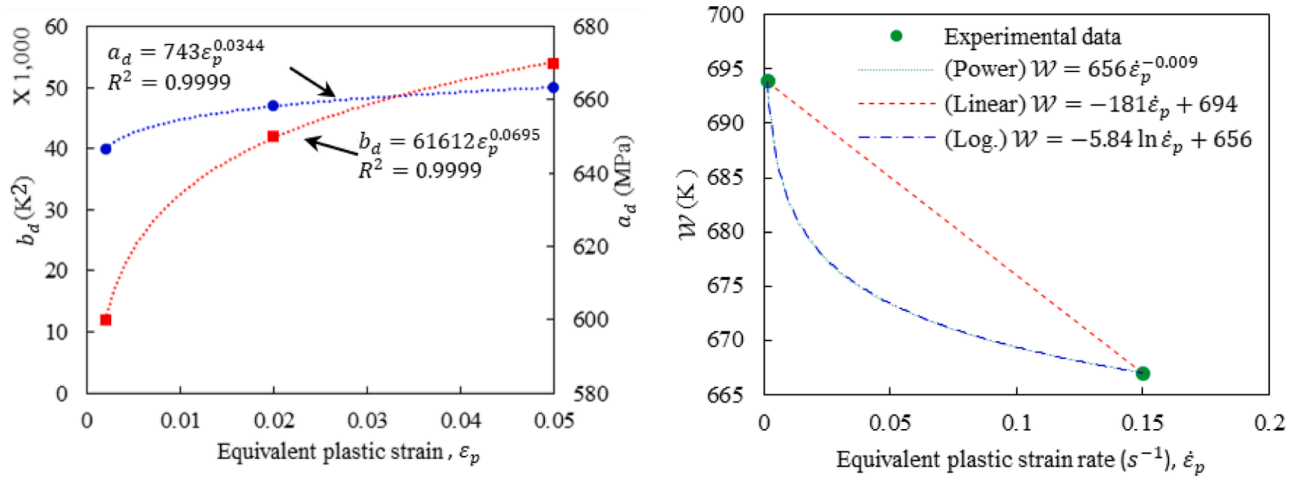

Fig. 3. Determination of the DSA hardening components: (a) a power-law form is used to define a_d and b_d as a function of equivalent plastic strain, i.e. $a_d = 743\varepsilon_p^{0.0344}$ (MPa) and $b_d = 61612\varepsilon_p^{0.0695}$ (K^2), whereas (b) various forms are employed to define $\mathscr{W}$ as a function of equivalent plastic strain rate. In the current work, a power-law form is utilized as follows: $\mathscr{W} = 656\dot{\varepsilon}_p^{-0.009}$ (K). The experimental data from [1] are indicated by dots.

$$\text{HARD(1)};\quad \frac{\partial\sigma\left(\varepsilon_p,\ \dot{\varepsilon}_p,\ T\right)}{\partial\varepsilon_p} = \frac{\partial\sigma_a\left(\varepsilon_p\right)}{\partial\varepsilon_p} + \frac{\partial\sigma_{th}\left(\varepsilon_p,\ \dot{\varepsilon}_p,\ T\right)}{\partial\varepsilon_p} + \frac{\partial\sigma_d\left(\varepsilon_p,\ \dot{\varepsilon}_p,\ T\right)}{\partial\varepsilon_p} \tag{19}$$

where,

$$\frac{\partial\sigma_a\left(\varepsilon_p\right)}{\partial\varepsilon_p} = n_1 B\varepsilon_p^{(n_1-1)} \tag{20}$$

$$\frac{\partial\sigma_{th}\left(\varepsilon_p,\ \dot{\varepsilon}_p,\ T\right)}{\partial\varepsilon_p} = n_2\overline{\sigma}_{th}\varepsilon_p^{(n_2-1)}\left(1-\left(\beta_1 T-\beta_2 T\frac{\dot{\varepsilon}_p}{\dot{\varepsilon}_p^0}\right)^{\frac{1}{q}}\right)^{\frac{1}{p}} \tag{21}$$

$$\frac{\partial\sigma_d\left(\varepsilon_p,\ \dot{\varepsilon}_p,\ T\right)}{\partial\varepsilon_p} = exp\left[-\frac{\left\{T-\mathscr{W}\left(\dot{\varepsilon}_p\right)\right\}^2}{b_d\left(\varepsilon_p\right)}\right]\left\{\frac{\partial a_d\left(\varepsilon_p\right)}{\partial\varepsilon_p} + a_d\left(\varepsilon_p\right)\frac{\left\{T-\mathscr{W}\left(\dot{\varepsilon}_p\right)\right\}^2}{b_d^2\left(\varepsilon_p\right)}\frac{\partial b_d\left(\varepsilon_p\right)}{\partial\varepsilon_p}\right\} \tag{22}$$

The definition of HARD(2) can be addressed by decomposing it into:

$$\text{HARD(2)};\quad \frac{\partial\sigma\left(\varepsilon_p,\ \dot{\varepsilon}_p,\ T\right)}{\partial\dot{\varepsilon}_p} = \frac{\partial\sigma_a\left(\varepsilon_p\right)}{\partial\dot{\varepsilon}_p} + \frac{\partial\sigma_{th}\left(\varepsilon_p,\ \dot{\varepsilon}_p,\ T\right)}{\partial\dot{\varepsilon}_p} + \frac{\partial\sigma_d\left(\varepsilon_p,\ \dot{\varepsilon}_p,\ T\right)}{\partial\dot{\varepsilon}_p} \tag{23}$$

where,

$$\frac{\partial\sigma_a\left(\varepsilon_p\right)}{\partial\dot{\varepsilon}_p} = 0 \tag{24}$$

$$\frac{\partial\sigma_{th}\left(\varepsilon_p,\ \dot{\varepsilon}_p,\ T\right)}{\partial\dot{\varepsilon}_p} = \frac{\overline{\sigma}_{th}\varepsilon_p^{n_2}\beta_2 T}{pq\dot{\varepsilon}_p^0}\left(\beta_1 T-\beta_2 T\frac{\dot{\varepsilon}_p}{\dot{\varepsilon}_p^0}\right)^{\frac{1-q}{q}}\left[1-\left(\beta_1 T-\beta_2 T\frac{\dot{\varepsilon}_p}{\dot{\varepsilon}_p^0}\right)^{\frac{1}{q}}\right]^{\frac{1-p}{p}} \tag{25}$$

$$\frac{\partial\sigma_d\left(\varepsilon_p,\ \dot{\varepsilon}_p,\ T\right)}{\partial\dot{\varepsilon}_p} = 2a_d\left(\varepsilon_p\right)exp\left[-\frac{\left\{T-\mathscr{W}\left(\dot{\varepsilon}_p\right)\right\}^2}{b_d\left(\varepsilon_p\right)}\right]\frac{\left(T-\mathscr{W}\left(\dot{\varepsilon}_p\right)\right)}{b_d\left(\varepsilon_p\right)}\frac{\partial\mathscr{W}\left(\dot{\varepsilon}_p\right)}{\partial\dot{\varepsilon}_p} \tag{26}$$

The definition of HARD(3) can be addressed by decomposing it into:

$$\text{HARD(3)};\quad \frac{\partial\sigma\left(\varepsilon_p,\ \dot{\varepsilon}_p,\ T\right)}{\partial T} = \frac{\partial\sigma_a\left(\varepsilon_p\right)}{\partial T} + \frac{\partial\sigma_{th}\left(\varepsilon_p,\ \dot{\varepsilon}_p,\ T\right)}{\partial T} + \frac{\partial\sigma_d\left(\varepsilon_p,\ \dot{\varepsilon}_p,\ T\right)}{\partial T} \tag{27}$$

where,

$$\frac{\partial\sigma_a\left(\varepsilon_p\right)}{\partial T} = 0 \tag{28}$$

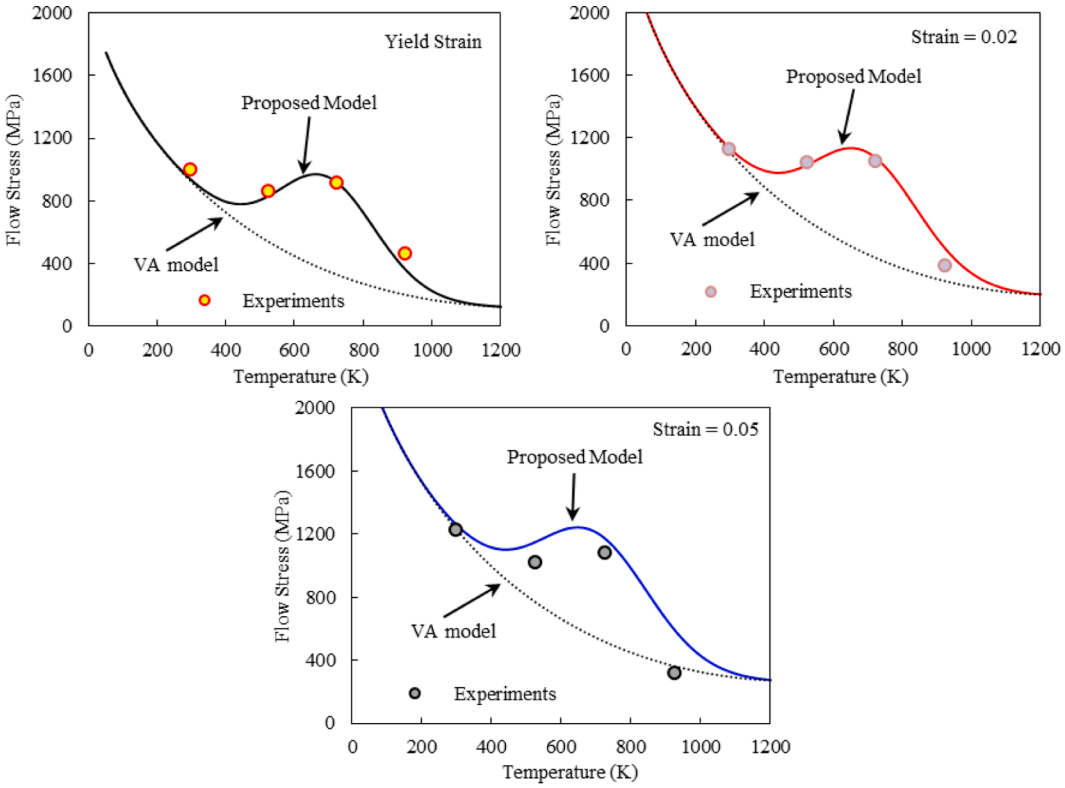

(a)

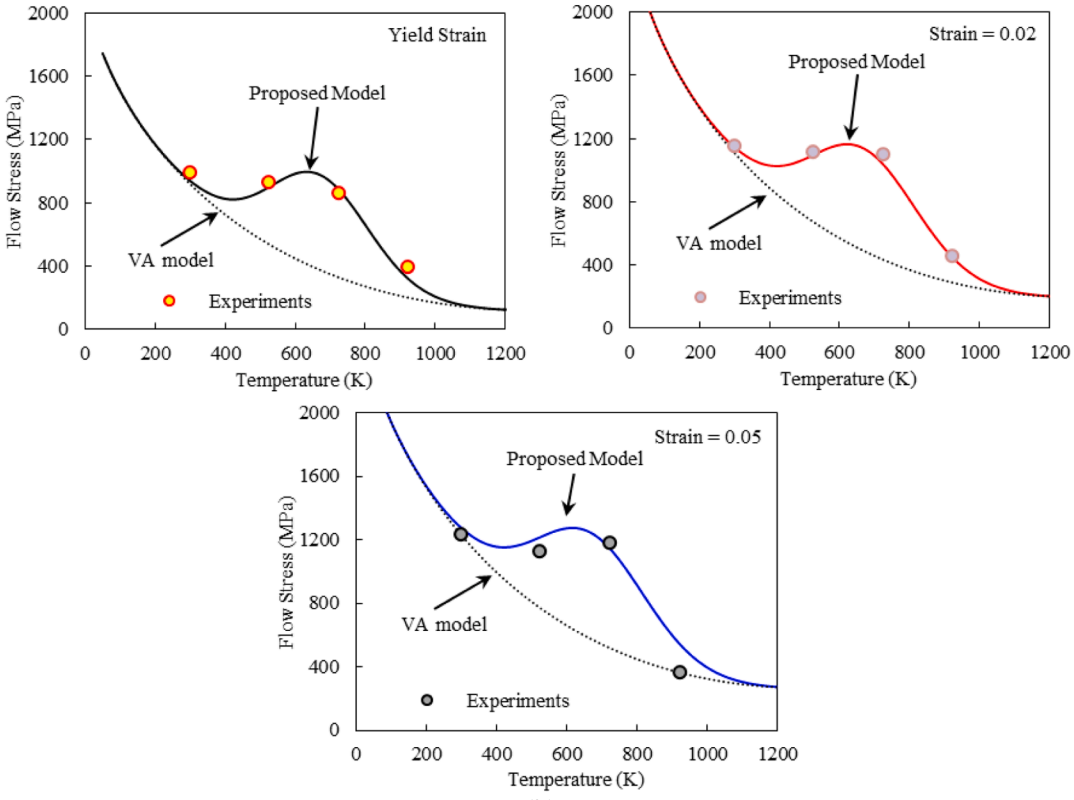

(b)

Fig. 4. Graphs of flow stress versus temperature at different strain levels from the VA model and the proposed model. The two different strain rates are applied: (a) $\dot{\varepsilon}_p = 0.0015$ and (b) $\dot{\varepsilon}_p = 0.15\ s^{-1}$. The experimental data [1] are indicated by dots. At a strain level of 0.05, the model predictions are a little off the experiments. This is because of the accumulation of damage observed in the experiments as shown in the stress-strain curves in Fig. 5. Note that the current model does not consider the damage effect.

$$\frac{\partial \sigma_{th}\left(\varepsilon_p,\ \dot{\varepsilon}_p,\ T\right)}{\partial T} = \frac{\overline{\sigma}_{th}\varepsilon_p^{n_2}}{p}\left(1-\left(\beta_1 T-\beta_2 T\frac{\dot{\varepsilon}_p}{\dot{\varepsilon}_p^o}\right)^{\frac{1}{q}}\right)^{\frac{1-p}{p}}\left(\frac{-1}{q}\left(\beta_1 T-\beta_2 T\frac{\dot{\varepsilon}_p}{\dot{\varepsilon}_p^o}\right)^{\frac{1-q}{q}}\right)\left(\beta_1-\beta_2\frac{\dot{\varepsilon}_p}{\dot{\varepsilon}_p^o}\right) \tag{29}$$

$$\frac{\partial \sigma_d\left(\varepsilon_p,\ \dot{\varepsilon}_p,\ T\right)}{\partial T} = 2a_d(\varepsilon_p)exp\left[-\frac{\left\{T-\mathscr{W}\left(\dot{\varepsilon}_p\right)\right\}^2}{b_d(\varepsilon_p)}\right]\frac{\left(\mathscr{W}\left(\dot{\varepsilon}_p\right)-T\right)}{b_d(\varepsilon_p)} \tag{30}$$

A simple uniaxial tension problem is solved to compute stress versus strain responses at various temperatures with the two strain rates. A single three-dimensional solid eight-node brick element (C3D8) is employed. The material parameters in Table 1 are used once again for the FE simulations. The obtained FEM results are shown in the next section via stress versus strain graphs to show its accuracy.

5. Stress-strain curves

Flow stress versus strain data is utilized in this section to verify the proposed model and the corresponding numerical algorithm developed in the previous section. The theoretical predictions from the proposed model, as well as the numerical calculations from the developed FE code, are plotted in Fig. 5 along with the experimental measurements from [1] under $\dot{\varepsilon}_p = 0.0015$ and $0.15s^{-1}$ at various temperatures. The VA model predictions are also shown for comparison. Fig. 5 clearly shows the disorder of flow stress about temperature caused by the DSA phenomenon because the flow stress at $T = 723K$ is almost the same with or slightly larger than the one at $T = 523K$ under both strain rates. At certain combinations of temperature and strain rate where DSA becomes functional, e.g., $T = 523K$ and $723K$ under both strain rates, the proposed model can clearly simulate accurately the experiments while the VA model cannot. The numerical predictions also show good agreements with experiments, particularly it is demonstrated that the developed FE code well describes the proposed constitutive model. Note that, in the early strain range in both strain rates, there is a gap between the experimental data and model predictions. This is because of the previously mentioned assumption of infinitesimal elastic deformation that was made for the derivation of the proposed model. On the contrary, the experiment showed a fair amount of elastic range, which naturally generates a gap between them.

Beyond a strain level of 0.03, softening is notably observed in the experiments, especially at $T = 523K$ and $723K$ under both strain rates. As indicated in Abed et al. [1], this is due to the accumulation of damage, which is initiated by a small crack network in materials. It should be noted that the current model is not a coupled damage-plasticity model, therefore it does not consider the damage effect.

Figs. 6 shows flow stress surfaces from the proposed model at a wide range of temperatures ranging from cryogenic to elevated temperatures. The experimental data illustrated by dots are located mostly near the surfaces in both strain rates.

It should be noted that stress versus strain graphs at high strain rates are not considered in Figs. 5 and 6. In Abed et al. [1], it was revealed from the experiments that the role of solute/dislocation interactions in not effective at the range of high strain rates, which in turn, dynamic strain aging might not be active in that range. In fact, this is the reason that the experimental data at $\dot{\varepsilon}_p = 0.0015$ and $0.15s^{-1}$ were considered only when the functional form of $\mathscr{W}$ is determined from the experimental data in Fig. 3(b).

6. Strain rate sensitivity (SRS)

Strain rate sensitivity (m) can be defined as a slope in stress versus logarithmic strain rate graph, i.e. $m = d\sigma/d\ln\dot{\varepsilon}$. At low strain rates, the dislocations continuously encounter obstacles when they move through the lattices, and the thermal activation energy (ΔG) lowers the effective barrier height for dislocation motion. Since ΔG decreases with strain rate and increases with temperature, the following equation can be used [59].

$$\Delta G = kT\ln\frac{\dot{\varepsilon}_0}{\dot{\varepsilon}} \tag{31}$$

where k is the Boltzmann constant and $\dot{\varepsilon}_0$ is the reference strain rate.

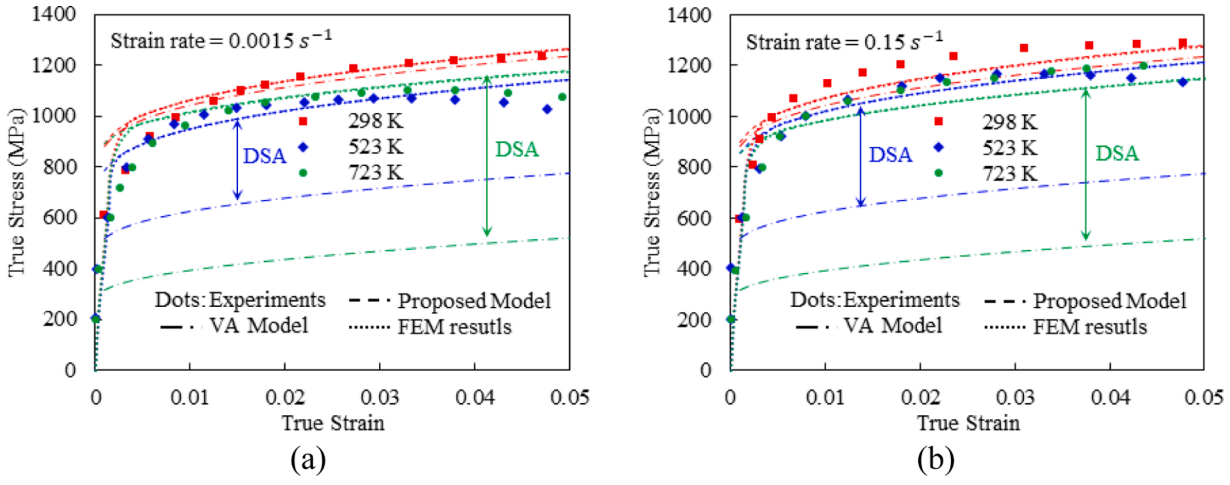

Fig. 5. Stress-strain predictions from the VA model, the proposed model and the FEM results with the experimental data [1] at the three temperatures (298, 523, and $723K$) under (a) $\dot{\varepsilon}_p = 0.0015$ and (b) $\dot{\varepsilon}_p = 0.15\ s^{-1}$. At elevated temperatures, i.e. 523 and $723K$, DSA becomes very active under both strain rates, as a result, the VA model is not able to provide a good quality of predictions. The DSA-induced hardening in those temperatures is well captured by the proposed model and the developed finite element code.

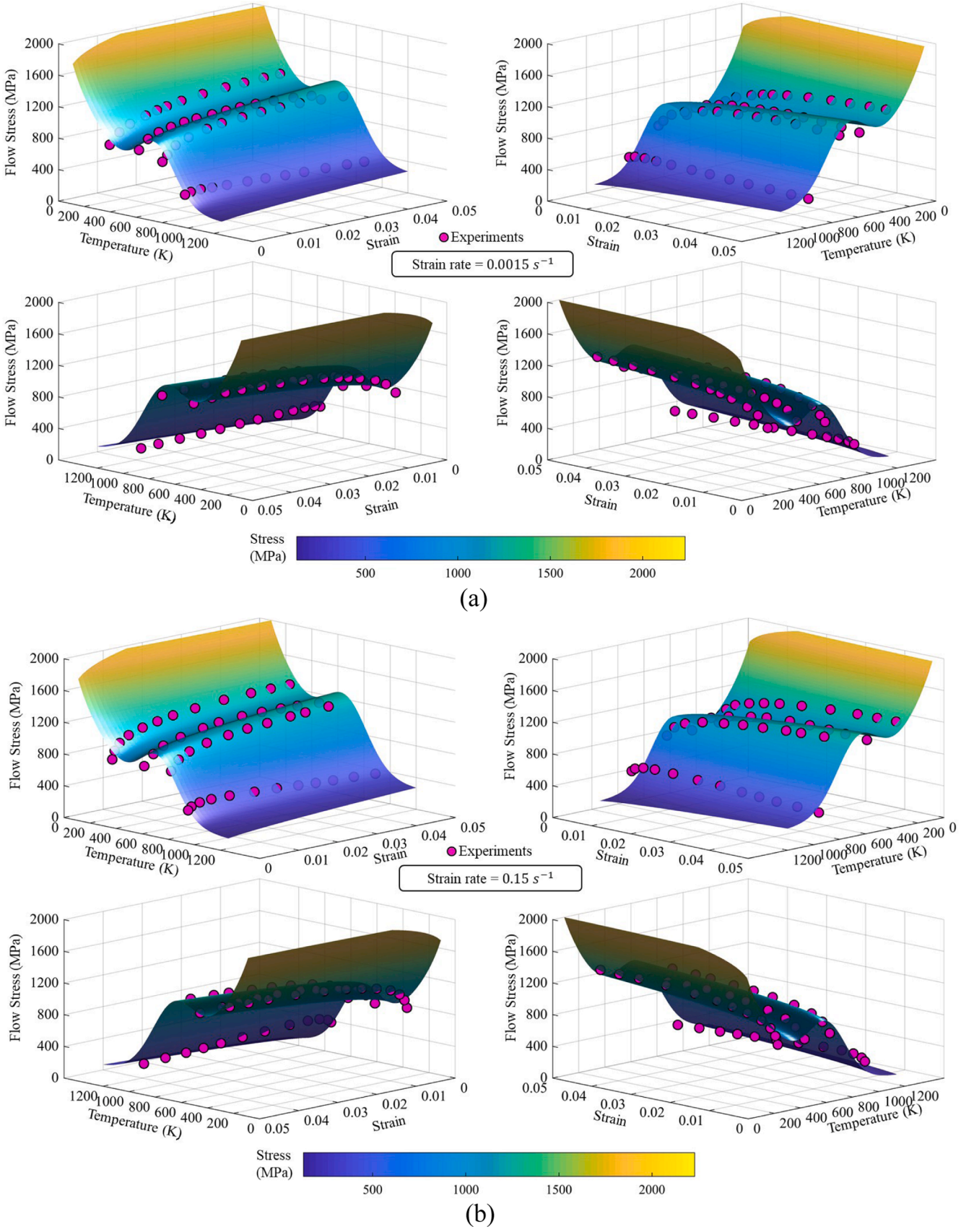

Fig. 6. Flow stress surfaces at a wide range of strains and temperatures: (a) $\dot{\varepsilon}_p = 0.0015$ and (b) $\dot{\varepsilon}_p = 0.15\ s^{-1}$. The experimental data [1] are indicated by dots. The dots are mostly placed near the surfaces. Without DSA, surfaces are supposed to constantly decrease with temperature increase. However, hardening due to DSA leads to bump-shape stress surfaces at a certain range of temperatures.

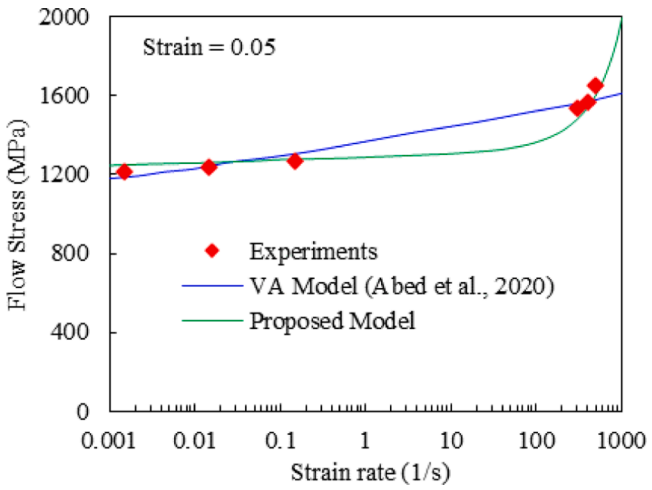

Fig. 7. Graph of flow stress as a function of strain rate in logarithmic scale at room temperature for a strain rate sensitivity analysis. The experimental data [1] are indicated by dots. The experiments show high strain rate sensitivity at high strain rates. The results from the VA model proposed in Abed et al. [1] do not accurately capture the experiments, especially at high strain rates. The proposed model, on the other hand, is able to capture the high strain rate sensitivity accurately.

As shown in this equation, ΔG decreases as $\dot{\varepsilon}$ increases since less time is available to get over the barriers. Thus, at low strain rates, ΔG becomes relatively higher, and more load is needed to overcome barriers. The effect of thermal activation is then entirely exploited, resulting in less external stress and lower SRS [62]. At high strain rates, on the other hand, ΔG is relatively small and not enough to overcome the obstacles. As a result, the effect of the thermal activation weakens gradually and results in larger external stress and higher SRS [59]. In addition, dislocations move much faster at high strain rates and these rapid-moving dislocations cause significant heat. It may be assumed that metals behave as Newtonian viscous materials with respect to dislocations. Thus, the motions of dislocations are subjected to viscous drag primarily from the interactions between dislocations and electron (electron viscosity) as well as dislocations and thermal vibrations (phonon drag). Consequently, this results in a much higher SRS.

Fig. 7 shows the stress versus logarithmic strain rate graph for MMFX at room temperature. It is clearly seen from the experiments that SRS becomes much more significant at high strain rates. The VA model in the literature was not able to capture this trend, whereas the proposed model shows a good agreement. The VA model in Abed et al. [1] included the term $\ln\dot{\varepsilon}_p/\dot{\varepsilon}_p^0$ instead of $\dot{\varepsilon}_p/\dot{\varepsilon}_p^0$ in Eq. (3) in the current work. Because of the mathematical reason, the models using the natural logarithmic term inherently result in the linear behavior with respect to x-axis in Fig. 7, which causes unrealistic results. To avoid it and to obtain a better agreement with the experimental measurements, the non-logarithmic term, $\dot{\varepsilon}_p/\dot{\varepsilon}_p^0$, is utilized in this work, which provides a good quality of results at the high strain rate range.

7. Conclusions

The constitutive model for MMFX is developed by considering the effect of the DSA-induced hardening. The functional form of a Weibull distribution probability density function is employed to model the bell-shaped hardening in flow stress versus temperature graphs. The model parameters are obtained from the step-by-step calibration process. Correspondingly, a finite element code is written to numerically verify the proposed model.

Since occurrence and characteristics of the DSA phenomenon depend on the level of plastic strain as well as the range of temperature and strain rate, the stress component for describing the DSA effect needs to be modeled as a function of equivalent plastic strain, equivalent plastic strain rate and temperature. In the proposed model, the magnitude of the DSA-induced hardening, the temperature range where DSA becomes active, and the temperature where the effect of DSA is strongest are related to the equivalent plastic strain are defined by the DSA stress component.

The proposed model showed a good agreement with the experiments at temperatures ranging from room temperature to $923K$ and strain rates ranging from 0.0015 to $500s^{-1}$. The VA model cannot capture the experiments without incorporating the DSA component at $T = 523K$ and $723K$ under $\dot{\varepsilon}_p = 0.0015\ s^{-1}$ and $0.15s^{-1}$ where DSA becomes pronounced. Meanwhile, damage accumulation was significantly observed beyond a strain of 0.03 in the stress-strain curves. In order to more accurately model the material behavior, the energy-based damage-plasticity constitutive model may be established as was done in the authors' previous work [57]. The effective stress can be expressed using the concept of undamaged and damaged material states as $\bar{\sigma} = \sigma/(1-\phi)$ where $\bar{\sigma}$, σ and φ denote the effective stress, stress of the damaged body, and the damage factor, respectively. The evolution of damage can be obtained using the energy-based model by Abed et al. [2].

The finite element code for the proposed model was also developed by building a user-defined subroutine and its validity is also tested using theoretical predictions from the proposed model as well as the experimental measurements. Using the validated numerical algorithm, some DSA-related phenomena such as the propagation of Lüders band may be further investigated in the future [26, 34, 48].

Declaration of Competing Interest

The authors declare that they have no known competing financial interests or personal relationships that could have appeared to influence the work reported in this paper.

Acknowledgment

The first and third authors acknowledge the financial support provided by a grant from the National Science Foundation EPSCoR CIMM (grant number #OIA-1541079).

References

[1] Abed F, Abdul-Latif A, Voyiadjis GZ. Performance of MMFX Steel Rebar at Elevated Temperatures. J Eng Mech 2020:146.
[2] Abed FH, Al-Tamimi AK, Al-Himairee RM. Characterization and Modeling of Ductile Damage in Structural Steel at Low and Intermediate Strain Rates. J Eng Mech-Asce 2012;138:1186–94.
[3] Alomari AS. Serrated yielding in austenitic stainless steels. Mater High Temp; 2021.
[4] Beese AM, Wang ZQ, Stoica AD, Ma D. Absence of dynamic strain aging in an additively manufactured nickel-base superalloy. Nat Commun 2018;9.
[5] Bergstrom Y, Roberts W. Dislocation Model for Dynamical Strain Ageing of Alpha-Iron in Jerky-Flow Region. Acta Metall Mater 1971;19:1243–51.
[6] Bobbili R, Madhu V. A modified Johnson-Cook model for FeCoNiCr high entropy alloy over a wide range of strain rates. Mater Lett 2018;218:103–5.
[7] Brechtl J, Chen SY, Lee C, Shi YZ, Feng R, Xie X, Hamblin D, Coleman AM, Straka B, Shortt H, Spurling RJ, Liaw PK. A review of the serrated-flow phenomenon and its role in the deformation behavior of high-entropy alloys. Metals 2020;10.
[8] Cai ZY, Wan M, Liu ZG, Wu XD, Ma BL, Cheng C. Thermal-mechanical behaviors of dual-phase steel sheet under warm-forming conditions. Int J Mech Sci 2017;126:79–94.
[9] Chen SY, Wang L, Li WD, Tong Y, Tseng KK, Tsai CW, Yeh JW, Ren Y, Guo W, Poplawsky JD, Liaw PK. Peierls barrier characteristic and anomalous strain hardening provoked by dynamic-strain-aging strengthening in a body-centered-cubic high-entropy alloy. Mater Res Lett 2019;7:475–81.
[10] Chen Y, Guo WT, Yang PP, Zhao JH, Guo ZY, Dong LT, Zhong Z. Constitutive modeling of neo-Hookean materials with spherical voids in finite deformation. Extreme Mech Lett 2018;24:47–57.
[11] Cottrell AH. A Note on the Portevin-Le Chatelier Effect. Philos Mag 1953;44:829–32.
[12] DeJong SJ, Heffernan PJ, MacDougall C. Periodic Overload Corrosion Fatigue of MMFX and Stainless Reinforcing Steels. J Mater Civil Eng 2009;21:1–9.

[13] Dornelas VM, Oliveira SA, Savi MA, Pacheco PMCL, de Souza LFG. Fatigue on shape memory alloys: Experimental observations and constitutive modeling. Int J Solids Struct 2021;213:1–24.
[14] Dougherty L, Cerreta E, Gray G, Trujillo C, Lopez M, Vecchio K, et al. Mechanical behavior and microstructural development of low-carbon steel and microcomposite steel reinforcement bars deformed under quasi-static and dynamic shear loading. Metall Mater TransA 2009;40:1835–50.
[15] El-Hacha R, El-Agroudy H, Rizkalla SH. Bond characteristics of high-strength steel reinforcement. Aci Struct J 2006;103:771–82.
[16] Epperly EN, Sills RB. Transient solute drag and strain aging of dislocations. Acta Mater 2020;193:182–90.
[17] Follansbee PS. Further Analysis of Dynamic Strain Aging in Context of an Internal State Variable Constitutive Formalism. Metall Mater Trans A 2020;51:1275–85.
[18] Frost M, Jury A, Heller L, Sedlak P. Experimentally validated constitutive model for NiTi-based shape memory alloys featuring intermediate R-phase transformation: A case study of Ni48Ti49Fe3. Mater Design 2021:203.
[19] Gong L, Darwin D, Browning JP, Locke Jr CE. Evaluation of mechanical and corrosion properties of MMFX reinforcing steel for concrete. Kansas. Dept. of Transportation. 2004.
[20] Graff S, Forest S, Strudel JL, Prioul C, Pilvin P, Bechade JL. Strain localization phenomena associated with static and dynamic strain ageing in notched specimens: experiments and finite element simulations. Mat Sci Eng a-Struct 2004;387:181–5.
[21] Graff S, Forest S, Strudel JL, Prioul C, Pilvin P, Bechade JL. Finite element simulations of dynamic strain ageing effects at V-notches and crack tips. Scripta Mater 2005;52:1181–6.
[22] Guo ZY, Caner F, Peng XQ, Moran B. On constitutive modelling of porous neo-Hookean composites. J Mech Phys Solids 2008;56:2338–57.
[23] Guo ZY, Chen Y, Wan Q, Li HT, Shi XH, Tang S, Peng XQ. A Hyperelastic Constitutive Model for Chain-Structured Particle Reinforced Neo-Hookean Composites. Mater Design 2016;95:580–90.
[24] Jenab A, Taheri AK. Experimental investigation of the hot deformation behavior of AA7075: Development and comparison of flow localization parameter and dynamic material model processing maps. Int J Mech Sci 2014;78:97–105.
[25] Joun MS, Lee HJ, Lim SG, Lee KH, Cho GS. Dynamic strain aging of an AISI 1025 steel coil and its relationship with macroscopic responses during the upsetting process. Int J Mech Sci 2021:200.
[26] Keralavarma SM, Bower AF, Curtin WA. Quantum-to-continuum prediction of ductility loss in aluminium-magnesium alloys due to dynamic strain aging. Nat Commun 2014;5.
[27] Komarasamy M, Alagarsamy K, Mishra RS. Serration behavior and negative strain rate sensitivity of Al0.1CoCrFeNi high entropy alloy. Intermetallics 2017;84:20–4.
[28] Kozlowska A, Grzegorczyk B, Morawiec M, Grajcar A. Explanation of the PLC Effect in Advanced High-Strength Medium-Mn Steels. A review. Materials 2019;12.
[29] le Graverend JB, Lee S. Phenomenological modeling of the effect of oxidation on the creep response of Ni-based single-crystal superalloys. Extreme Mech Lett 2020:39.
[30] Lejon J, Wang BC, Kari L. A constitutive model of the dynamic shear modulus dependence on temperature, prestrain, dynamic strain amplitude and magnetic field for magneto-sensitive elastomer. Int J Solids Struct 2021;219:106–19.
[31] Li DH, Shang DG, Li ZG, Wang JJ, Hui J, Liu XD, Tao ZQ, Zhang CC, Chen B. Unified viscoplastic constitutive model under axial-torsional thermo-mechanical cyclic loading. Int J Mech Sci 2019;150:90–102.
[32] Mannan SL, Valsan M. High-temperature low cycle fatigue, creep-fatigue and thermomechanical fatigue of steels and their welds. Int J Mech Sci 2006;48:160–75.
[33] Mansouri MR, Fuchs PF, Criscione JC, Schrittesser B, Beter J. The contribution of mechanical interactions to the constitutive modeling of fiber-reinforced elastomers. Eur J Mech a-Solid 2021:85.
[34] Marchenko A, Maziere M, Forest S, Strudel JL. Crystal plasticity simulation of strain aging phenomena in alpha-titanium at room temperature. Int J Plasticity 2016;85:1–33.
[35] Maziere M, Mortensen A, Forest S. Finite element simulation of the Portevin-Le Chatelier effect in highly reinforced metal matrix composites. Philos Mag 2021;101:1471–89.
[36] Mccormick PG. Theory of Flow Localization Due to Dynamic Strain Aging. Acta Metall Mater 1988;36:3061–7.
[37] Meng C, Hu W, Sandlobes S, Korte-Kerzel S, Gottstein G. The effect of large plastic deformation on elevated temperature mechanical behavior of dynamic strain aging Al-Mg alloys. Acta Mater 2019;181:67–77.
[38] Meng Q, Shi X. A microstructure-based constitutive model of anisotropic cellulose nanopaper with aligned nanofibers. Extreme Mech Lett 2021;43:101158.
[39] Mesarovic SD. Dynamic strain aging and plastic instabilities. J Mech Phys Solids 1995;43:671–700.
[40] Metwally IM, Ghannam M. Behaviour of green ultra-high-performance concrete beams with corrosion resistant alloy steel (MMFX) bars. SN Applied Sciences 2020;2:1–14.
[41] Mohamed N, Boulfiza M, Evitts R. Corrosion of Carbon Steel and Corrosion-Resistant Rebars in Concrete Structures Under Chloride Ion Attack. J Mater Eng Perform 2013;22:787–95.
[42] Nam JH, Oh SK, Park MH, Lee YK. The mechanism of dynamic strain aging for type A serrations in tensile curves of a medium-Mn steel. Acta Mater 2021:206.
[43] Nemat-Nasser S, Guo WG, Cheng JY. Mechanical properties and deformation mechanisms of a commercially pure titanium. Acta Mater 1999;47:3705–20.
[44] Nguyen QK, Deng FH, Zhang P. Temperature and rate dependent constitutive behaviors of low melt Field's metal. Extreme Mech Lett 2020:37.
[45] Oh SK, Kilic ME, Seol JB, Hong JS, Soon A, Lee YK. The mechanism of dynamic strain aging for type A serrations in tensile flow curves of Fe-18Mn-0.55C (wt.%) twinning-induced plasticity steel. Acta Mater 2020;188:366–75.
[46] Picu RC. A mechanism for the negative strain-rate sensitivity of dilute solid solutions. Acta Mater 2004;52:3447–58.
[47] Sitko M, Skoczen B, Wroblewski A. FCC-BCC phase transformation in rectangular beams subjected to plastic straining at cryogenic temperatures. Int J Mech Sci 2010;52:993–1007.
[48] Song RH, Qin HL, Bi ZN, Zhang J, Chi H, Busso EP, et al. Experimental and numerical investigations of dynamic strain ageing behaviour in solid solution treated Inconel 718 superalloy. Eng Comput. 2021;38:19–35.
[49] Song Y, Garcia-Gonzalez D, Rusinek A. Constitutive Models for Dynamic Strain Aging in Metals: Strain Rate and Temperature Dependences on the Flow Stress. Materials 2020;13:1794.
[50] Song Y, Peterson W. Theoretical Study for Dynamic Strain Aging in Niobium: Effect of Temperature and Strain Rate on the Flow Stress. Met Mater Int 2020:1–14.
[51] Song Y, Voyiadjis GZ. Constitutive modeling of dynamic strain aging for HCP metals. Eur J Mech a-Solid 2020;83:104034.
[52] Sumpter MS, Rizkalla SH, Zia P. Behavior of High-Performance Steel as Shear Reinforcement for Concrete Beams. Aci Struct J 2009;106:171–7.
[53] Taylor GI. Plastic strain in metals. J I Met 1938;62:307–24.
[54] Venkata SP, Cui K, Guo J, Zehnder AT, Gong J, Hui C-Y. Constitutive modeling of bond breaking and healing kinetics of physical Polyampholyte (PA) gel. Extreme Mech Lett 2021:101184.
[55] Voyiadjis GZ, Abed FH. Microstructural based models for bcc and fcc metals with temperature and strain rate dependency. Mech Mater 2005;37:355–78.
[56] Voyiadjis GZ, Song Y. A physically based constitutive model for dynamic strain aging in Inconel 718 alloy at a wide range of temperatures and strain rates. Acta Mech 2020;231:19–34.
[57] Voyiadjis GZ, Song Y, Rusinek A. Constitutive model for metals with dynamic strain aging. Mech Mater 2019;129:352–60.
[58] Wang JJ, Guo WG, Gao XS, Su J. The third-type of strain aging and the constitutive modeling of a Q235B steel over a wide range of temperatures and strain rates. Int J Plasticity 2015;65:85–107.
[59] Wang L, Qiao JW, Ma SG, Jiao ZM, Zhang TW, Chen G, Zhao D, Zhang Y, Wang ZH. Mechanical response and deformation behavior of Al0.6CoCrFeNi high-entropy alloys upon dynamic loading. Mat Sci Eng a-Struct 2018;727:208–13.
[60] Wang LF, Feng PH, Xing XG, Wu Y, Liu ZS. A one-dimensional constitutive model for NiTi shape memory alloys considering inelastic strains caused by the R-phase transformation. J Alloy Compd 2021:868.
[61] Zhang LH, Pellegrino A, Townsend D, Petrinic N. Thermomechanical constitutive behaviour of a near alpha titanium alloy over a wide range of strain rates: Experiments and modelling. Int J Mech Sci 2021:189.
[62] Zhang TW, Jiao ZM, Wang ZH, Qiao JW. Dynamic deformation behaviors and constitutive relations of an AlCoCr1.5Fe1.5NiTi0.5 high-entropy alloy. Scripta Mater 2017;136:15–9.
[63] Zhao Y, Dezerald L, Pozuelo M, Zhou XR, Marian J. Simulating the mechanisms of serrated flow in interstitial alloys with atomic resolution over diffusive timescales. Nat Commun 2020:11.
[64] Zhong DM, Xiang YH, Liu JJ, Chen Z, Zhou HF, Yu HH, Qu SX, Yang W. A constitutive model for multi network elastomers pre-stretched by swelling. Extreme Mech Lett 2020:40.
[65] Zhou YH, Ou YC, Lee GC, O'Connor JS. Mechanical and low-cycle fatigue behavior of stainless reinforcing steel for earthquake engineering applications. Earthq Eng Eng Vib 2010;9:449–57.